19ᵉ Journées de l'Hydrodynamique
26 – 28 novembre 2024, Nantes

Development of a Coupled FSI Solver Based on OpenFOAM Overset Zone, PreCICE and Calculix: a Case Study for Energy Harvesting Applications using Flexible Flapping Foils

Karim Ahmed[(1)], Ludovic Chatellier[(1)], Ferdinando Auricchio[(2)], Alessandro Reali[(2)]

karim.ahmed@univ-poitiers.fr ; ludovic.chatellier@univ-poitiers.fr

ferdinando.auricchio@unipv.it; alessandro.reali@unipv.it

[(1)]INSTITUT P' département FTC équipe HYDEE, Université de Poitiers

[(2)]Department of Civil Engineering and Architecture (DICAr), University of Pavia

Summary

The influence of wing deformation on animal propulsion and movement is a fascinating topic that has sparked significant interest in biomimetics across academic and industrial fields. This research addresses these complex dynamics by developing an advanced numerical tool that enables detailed analysis of biological motion in fluid environments. This initiative is crucial for advancing our understanding of fluid-structure interaction (FSI) phenomena and facilitating the design of hydroelastic energy harvesters. To investigate these dynamics, we developed a flexible approach that integrates advanced numerical tools for fluid-structure interaction analysis. Using a mesh motion tool based on a modified overset technique, this method incorporates the OpenFOAM fluid dynamics solver and the CalculiX structural solver, creating a comprehensive framework capable of capturing and analyzing the intricate fluid and solid interactions present in biological motion. The reliability of this modified overset solver is validated through application to propulsion generation scenarios, specifically with a flapping foil case study, and by comparing the outcomes to established results in the literature [5] [18]. Additionally, this coupled FSI solver underwent critical validation by solving the benchmark Turek-Hron problem, demonstrating complete agreement with published results in [34]. We applied the solver to active-passive foils, incorporating active heaving motion and passive deformation. The results highlighted the significant impact of flexibility on energy harvesting. In a test case with a material of ($E = 26\ MPa$) and density ($\rho = 1220\ Kg/m^3$), we observed a 16.3% improvement in energy harvesting efficiency compared to a solid foil.

I – Introduction

The study of motion mechanisms in biological systems has drawn significant attention in biomimetics, with strong potential for energy harvesting applications. Driven by demand for sustainable solutions in aviation and maritime sectors, researchers have replicated bio-inspired systems. Literature explores the aerodynamics and hydrodynamics of natural systems [31, 38], applying insights to areas like energy harvesting [21], propulsion [14], and transportation [17]. The flapping motion in insects and birds, combining pitch, heave, and membrane deformation, inspires engineering devices for energy harvesting and propulsion [16].

Expanding on biomimetic applications, the global energy crisis underscores the need to move from fossil and nuclear fuels to renewable sources. Rising fuel costs and the risks of nuclear energy amplify interest in natural flow energy, like wind, tides, and marine currents, as eco-friendly energy solutions. Ocean energy, including tidal and wave power, holds promise as a reliable renewable energy source. Ocean currents and waves, with an average wave power density of 2–3 kW/m^2 below the surface [13], have substantial potential to contribute to global energy needs.

Harnessing ocean energy requires advanced numerical modeling to simulate the energy extraction process. To achieve this, we developed the *oversetZoneFvMesh*, enhancing OpenFOAM's overset capabilities for accurate fluid-structure interaction simulations under hydrodynamic forces. Documentation of the modifications and validation tests for this tool, including parallelization strategies and convergence studies, is available in [4]. Current efforts focus on integrating CalculiX for structural analysis using preCICE, advancing simulation capabilities for flexible, flapping hydrofoils and energy harvesting. Our "Coupled-OversetZone-preCICE-CalculiX" solver, validated through large amplitude heaving motion tests, demonstrates effective interaction with the overset mesh and accurate force coefficient calculations under varied amplitudes, in agreement with established results [5, 18].

Our analysis on active-passive foils for energy harvesting at Reynolds number $R_e = 20,000$, reduced frequency $k = 1$, heaving amplitude $h_0/c = 1$, and angle of attack $\alpha = 0°$, explored how material flexibility influences efficiency. Using PET ($E = 5.2$ GPa) we observed a 3.93% efficiency increase over the rigid case. More flexible materials like TPU ($E = 26$ MPa) increased efficiency by 11.69%, while an even more flexible material ($E = 5$ MPa) achieved a 22.78% increase, highlighting material flexibility's role in enhancing energy harvesting performance.

II – Overset zone Approach

The numerical treatment of moving flexible bodies in fluid solvers can be achieved using fixed or moving meshes, depending on how boundaries are controlled. Moving meshes adjust node positions to follow boundaries, requiring reprocessing at each time step, while fixed meshes maintain static nodes, using marker functions to track boundary motion. Simulating flexible flapping motion with dynamic meshes is complex due to combined patch deformation, heaving, and rotation. Small amplitude motions and minor deformations are effectively handled using the Arbitrary Lagrangian-Eulerian (ALE) method [20], as demonstrated in studies [15, 22, 23]. However, handling larger motions with both rotation and heaving can expose the limits of deformable moving meshes, leading to mesh distortion, increased non-orthogonality, and numerical instability.

To address these challenges, the overset mesh methodology offers a robust alternative, allowing for the simulation of arbitrary rigid body motions that would otherwise be difficult to achieve with traditional mesh deformation techniques. OpenFOAM has recently integrated overset mesh functionality into its dynamic mesh framework, facilitating more complex simulations involving body motion. Studies have explored the performance of this technique within OpenFOAM, such as the work by Laws et al. [25], which applied the overset mesh approach to a stationary foil benchmark problem and validated the computational outcomes against experimental data to evaluate accuracy.

The overset, or Chimera, method was introduced to the CFD community in the early 1980s by Atta [6] and further developed by Benek et al. [10, 8, 9]. Figure (1a) shows an overset grid slice for a foil, comprising a primary background mesh with overlapping front meshes. This setup simplifies mesh generation by removing boundary constraints, allowing structured or unstructured meshes to accommodate complex geometries without mesh interfaces. However, interpolation is needed to maintain connectivity between overlapping zones [7]. In the overset method, background and front meshes operate independently : in the background domain, cells corresponding to the front domain are treated as voids, while boundary values from the front mesh are interpolated into the background. The front mesh uses a similar process. At each time step, cells are classified into calculated cells (where equations are solved), interpolated cells (receiving values from neighboring cells), and holes (excluded from the solution), as shown in Figure (1b) [33].

(a) Overset mesh components
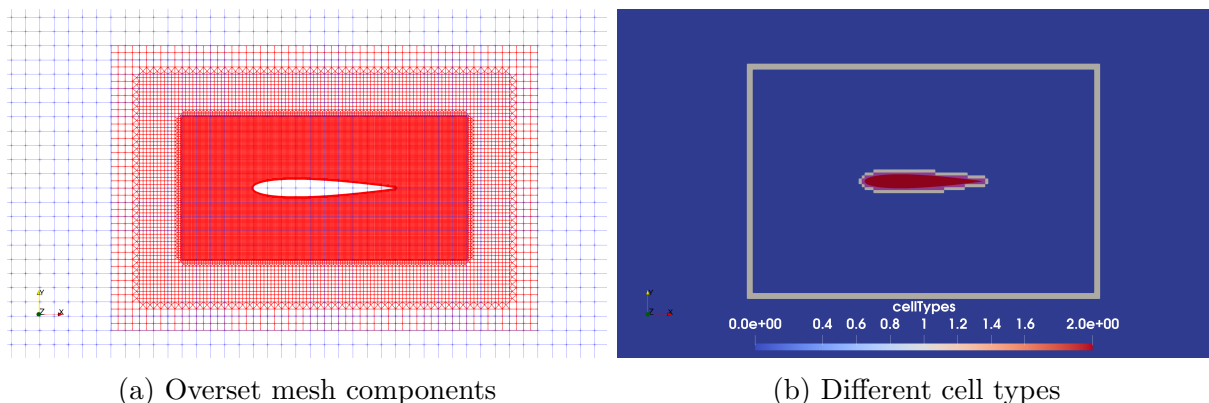
(b) Different cell types

FIGURE 1 – (a) Overset mesh components : the blue mesh represents the background, the red mesh is the front mesh with motion, and interpolation occurs in the overlapped region. (b) Cell types : red cells are holes, grey cells are interpolated, and blue cells are calculated, ordered by type as 2, 1, and 0, respectively.

In this study, we extend our previous work [4], where we developed an enhanced method combining mesh deformation with rigid body motion in overset meshes. While OpenFOAM's default overset capability supports a variety of applications, it faces challenges in scenarios requiring simultaneous motions. Generally, OpenFOAM's overset framework allows solid body motion in either the front or background mesh and supports patch displacement only in the front mesh. However, it does not facilitate concurrent patch displacement and solid body motion within the same mesh configuration. To address this limitation, we introduced the *dynamicOversetZoneFvMesh* solver, which enables both rigid body motion and selective patch deformation within specified zones. Figure (2c) shows leading-edge (LE) and trailing-edge (TE) deformation on a flapping foil, where for simplicity, the default overset applies coded displacement to the airfoil patch rather than a full fluid-structure interaction (FSI) setup. The primary constraint of the standard overset

method is that it applies motion and deformation across the entire mesh, rather than limiting these effects to the front mesh while keeping the background mesh fixed. The newly developed *dynamicOversetZoneFvMesh* solver, demonstrated in Figure (2d), overcomes this issue by enabling selective rigid body motion and localized deformation.
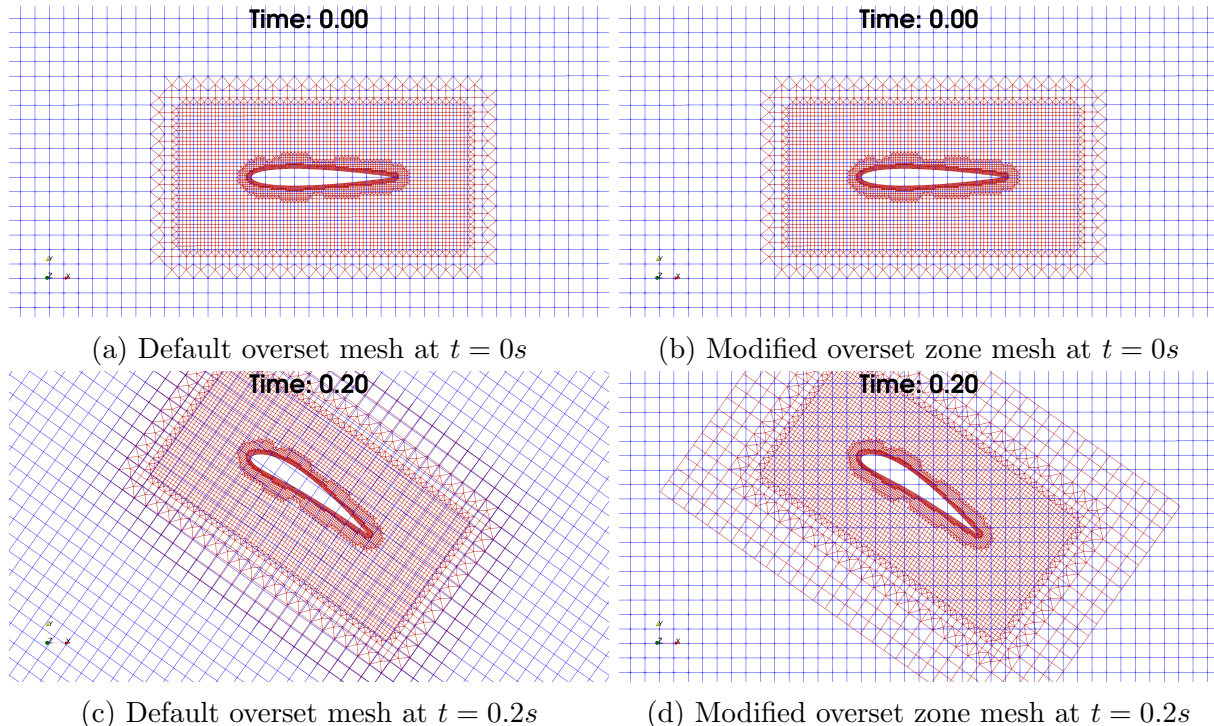

(a) Default overset mesh at $t = 0s$ (b) Modified overset zone mesh at $t = 0s$

(c) Default overset mesh at $t = 0.2s$ (d) Modified overset zone mesh at $t = 0.2s$

FIGURE 2 – (a,c) Mesh motion and patch deformation with the standard overset mesh, where motion applies to both meshes due to the absence of zone identification in the default solver. (b,d) Using the modified *dynamicOversetZoneFvMesh* solver, patch deformation is limited to the front mesh near the leading and trailing edges, while a rigid body motion is applied to the entire front mesh, keeping the background mesh stationary.

III – Fluid structure interaction Coupling

Achieving an accurate aero-elastic solution that combines flapping motion and foil flexibility requires coupling fluid dynamics with structural mechanics. This process involves the exchange of boundary conditions between fluid and structural models, with data flowing bidirectionally for effective interaction. In cases of strong coupling, multiple sub-iterations may be necessary to ensure boundary data consistency.

In this work, we use a partitioned approach, where the fluid and structural domains are managed independently by solvers specialized for each system, functioning as "black boxes" focused solely on coupling interface fields. This strategy leverages the strengths of each solver while keeping the coupling method streamlined.

The fluid dynamics are managed using OpenFOAM's *overPimpleDyMFoam* solver, which integrates the PIMPLE algorithm for solving unsteady Reynolds-Averaged Navier-Stokes (URANS) equations with an overset zone solver to handle mesh motion and deformation. The PIMPLE algorithm merges PISO and SIMPLE methods, with inner loops for velocity corrections and outer loops for pressure updates [32]. For structural analysis, we use CalculiX, an open-source finite element analysis (FEA) tool that supports both linear and non-linear simulations, providing flexibility for complex structural responses.

Data exchange between the fluid and structural solvers is managed by the open-source library preCICE, which enables interoperability between solvers across different physics and mesh structures. Minimal code modifications are needed to integrate preCICE, as its high-level API is implemented through an adapter, facilitating smooth coupling (see Figure 3).
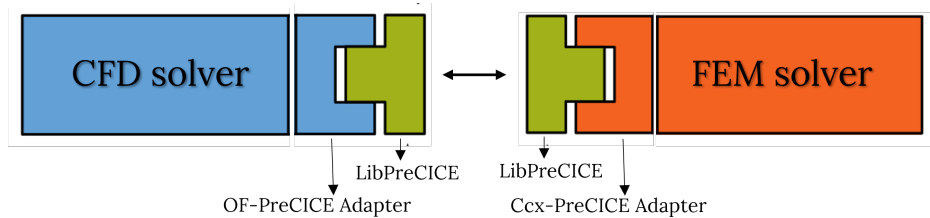

FIGURE 3 – Coupling between the fluid and solid solvers is facilitated by preCICE, which manages communication through specialized adapters. The process, adapted from [36], is illustrated in the diagram.

The OpenFOAM-preCICE adapter, developed by Gerasimos Chourdakis and Derek Risseeuw [11, 30], functions as a dynamic library and is implemented as an OpenFOAM function object, eliminating the need for OpenFOAM source code modifications. This function object interacts with the simulation at multiple stages, enabling the adapter to facilitate data exchange between the fluid simulation and preCICE.

The CalculiX-preCICE adapter, originally developed for fluid-structure interaction (FSI) by Alexander Rusch [36], operates on a similar principle, enabling communication between CalculiX and preCICE. Previous efforts successfully coupled standard OpenFOAM fluid solvers, such as `simpleFoam` and `pimpleFoam`, with CalculiX as the solid solver. However, coupling the `oversetZone` library, which involves two mesh zones (a front mesh and a background mesh), with a solid solver requires additional refinement. Consequently, several trials were conducted to establish reliable connections between the solvers across the distinct mesh zones. Following an extensive process of research and experimentation, the setup illustrated in Figure (4) represents the most effective configuration achieved for ensuring robust communication between the fluid and solid solvers.
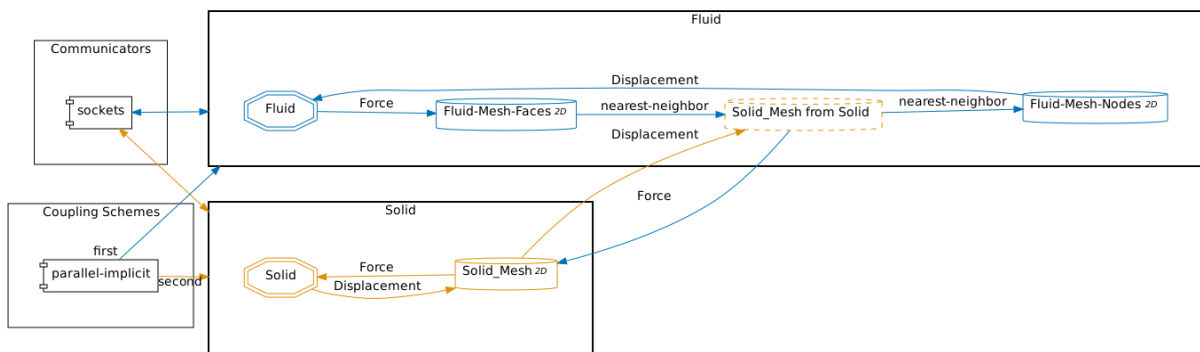

FIGURE 4 – The coupling configuration between the OpenFOAM (fluid) and CalculiX (solid) solvers via preCICE implements a parallel implicit scheme, with nearest-neighbor mapping for fluid-solid domain interaction, as shown in the diagram.

In this setup, the preCICE configuration outlines the coupling between a fluid and a solid solver, with color-coded loops and solver orders for clarity. The fluid solver loop (blue) includes two meshes : *Fluid-Mesh-Faces* for transferring *Force* data from the fluid

to the solid solver, and *Fluid-Mesh-Nodes* for receiving *Displacement* data from the solid solver. The solid solver loop (orange) uses a single mesh, *Solid-Mesh*, to both read *Force* data and write *Displacement* data.

Data mapping between meshes employs the nearest-neighbor method, aligning each point with its closest counterpart on the target mesh for accurate data transfer. Specifically, *Force* data maps from *Solid-Mesh* to *Fluid-Mesh-Faces*, while *Displacement* data maps from *Fluid-Mesh-Nodes* to *Solid-Mesh*, ensuring precise data alignment. Coupling is managed via a parallel implicit scheme, constrained by limits on iterations, relative convergence for *Force* and *Displacement*. To enhance convergence and ensure robust fluid-structure simulations, we apply an IQN acceleration method configured according to the settings in [3]. Key coupling parameters are detailed in Table (1).

Parameter	Value
Global time step (s)	5e-4
Maximum number of iterations for convergence	80
Convergence threshold for displacement (m)	1e-5
Convergence threshold for force (N)	5e-3

TABLE 1 – Parameters for the parallel implicit coupling scheme

IV – Coupled solver validation

To validate the coupling between fluid and solid solvers, we performed initial tests on the well-established Turek and Hron benchmark problem [34], a standard in FSI validation. This benchmark is sensitive to factors such as the Reynolds number, which influences the flow regime, and is complex due to high fluid density and viscosity paired with low structural stiffness, resulting in a tightly coupled system. The fluid domain setup, derived from [35], is shown in Figure (5). While the original benchmark tests multiple inflow speeds to evaluate different flow regimes around the cylinder with a flap, we focus on the FSI3 case due to its unsteady vortex-shedding flow, which effectively captures dynamic fluid-structure interactions. This case is modeled using URANS equations, addressing unsteady flow without additional turbulence modeling. The fluid and structural properties used are detailed in Table 2, and a parabolic inflow profile, gradually increasing over two seconds, is applied as in Equation (1).
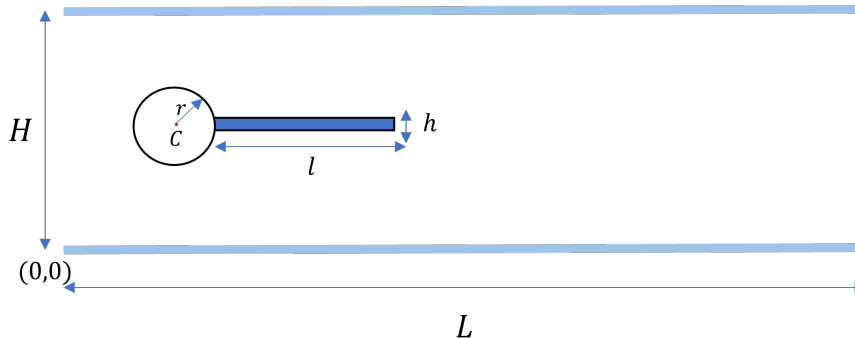

FIGURE 5 – The domain dimensions are L = 2.5 m and H = 0.41 m. Radius of Cylinder r = 0.05 m. For the elastic flap, l = 0.35 m and h = 0.02 m

Fluid	value	Structure	value
Density (ρ_f) [kg/m^3]	1,000	Density (ρ_s) [kg/m^3]	1,000
Viscosity (ν_f) [m^2/s]	10^{-3}	Young's modulus (E) [kg/m/s^2]	$5.6 \cdot 10^6$
Mean velocity (U) [m/s]	2	Poisson ratio (ν)	0.4
Reynolds number (Re)	200		

TABLE 2 – Fluid and structural parameters for Turek-Hron FSI3 case.

$$v^f(y) = \left(1.5\bar{U}\frac{4y(h-y)}{h^2}\right),$$

$$u(t,0,y) = \begin{cases} \left(\frac{1-\cos\left(\frac{\pi}{2}t\right)}{2}v^f, 0\right) & \text{if } t < 2 \text{ s} \\ (v^f, 0) & \text{if } t \geq 2 \text{ s} \end{cases} \tag{1}$$

To ensure a stable initiation of the fluid-structure interaction, the velocity profile is gradually ramped, with a zero velocity gradient applied at the outlet and non-slip boundary conditions imposed on the top, bottom, and cylinder with flap surfaces to enforce fluid adherence. The outlet pressure is fixed at zero, and a zero-gradient condition is specified throughout the remainder of the domain. Figures (6c) and (6d) show excellent agreement between our solver results and the literature for both vertical displacement and vertical force, validating the coupled FSI solver's capability to handle complex scenarios, including our primary objective of analyzing a flapping flexible hydrofoil.
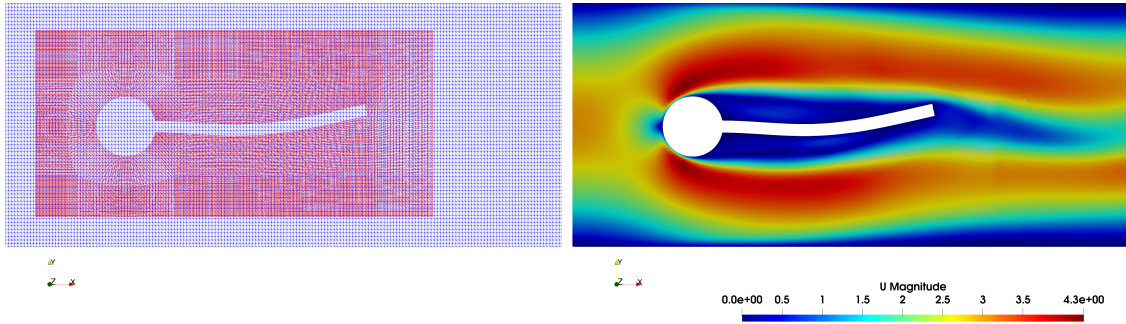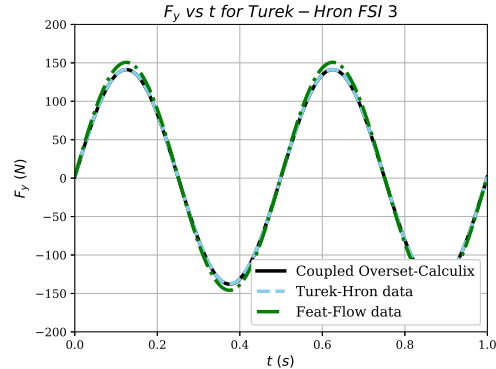

(a) Mesh representation

(b) Velocity contours
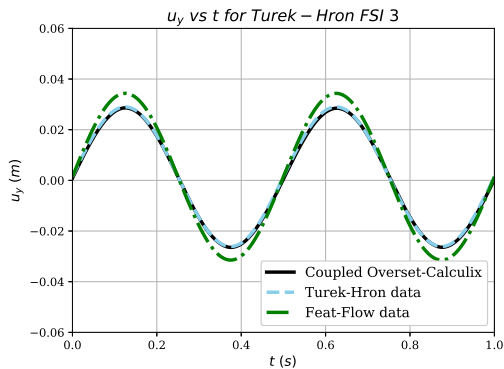
(c) The vertical displacement u_y at point A

(d) The vertical force F_y at point A

FIGURE 6 – (a),(b) Representation of the overset mesh and velocity contours. (c),(d) Results validation of our coupled solver with published data [35] and [2].

7

V – Heaving Foil Modelling

The previously validated FSI solver is applied to analyze the behavior of a flexible wing structure in fluid, focusing on the response of flexible foils under periodic motions. A 2D analysis will be conducted in two phases : first, by simulating a solid heaving foil based on the study by [29], which investigates how varying heaving amplitudes and frequencies affect propulsive efficiency. This phase aims to verify the solver's reliability for such an application. The second phase extends this analysis to flexible foils, examining how material properties and geometry influence the response to different heaving motions, with a particular emphasis on energy harvesting efficiency.

V – 1   Numerical Domain

V – 1.1   Fluid Domain

The airfoil model in this study is the NACA 0012, positioned within a rectangular computational domain measuring $20c$ in length and $12c$ in height, centered at the foil's heaving point, located at $c/3$ along the y-axis, as illustrated in Figure (7). The foil undergoes heaving motions in the x-y plane. Initial and boundary conditions for the incompressible laminar flow are specified in Table (3). Simulations ran for at least 25 seconds to establish a stable periodic flow with time steps adjusted based on heaving frequency and amplitude to ensure solution accuracy.
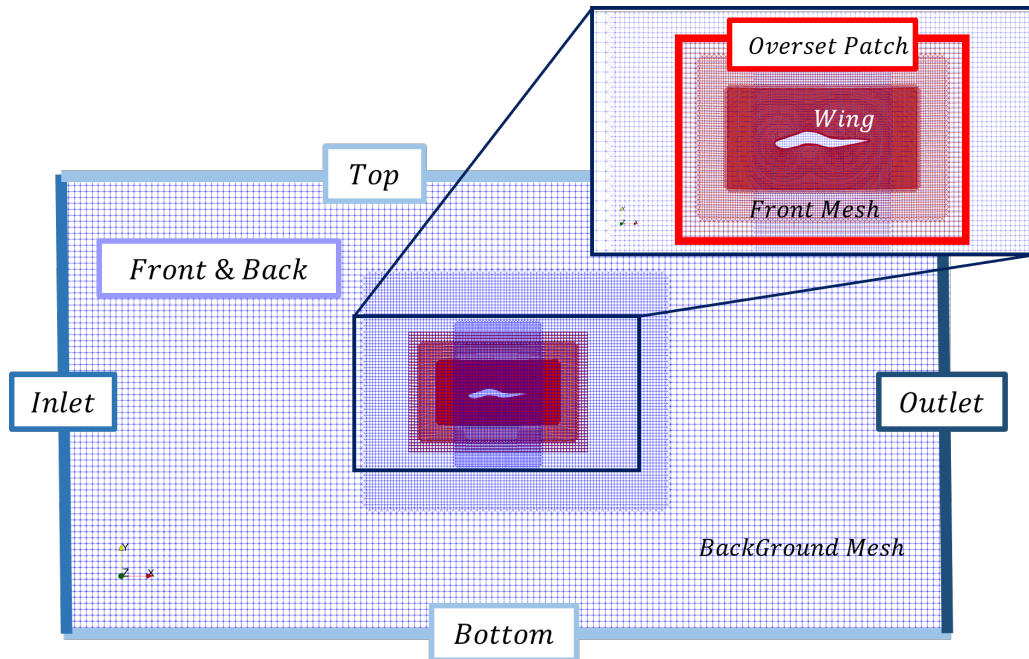

FIGURE 7 – The computational domain for the heaving foil problem, including the mesh configuration and the representation of various boundaries for both the front and background meshes.

Further Details on the meshing approach and mesh independence analysis are provided in our earlier publication [4]. The finite volume scheme and solution files (*fvScheme* and *fvSolution*), are constructed based on the best practices recommended by both the OpenFOAM community and Wolf Dynamics procedures [12].

| Boundary	P	U	*pointDisplacement*
Wing	zeroGradient	movingWallVelocity	fixedValue \$internalField
Inlet	zeroGradient	fixedValue	uniformFixedValue
Outlet	fixedValue	zeroGradient	uniformFixedValue
Top & Bottom	zeroGradient	uniformFixedValue	
Overset Patch		overset	
Front & Back		empty	

TABLE 3 – Boundary conditions for the fluid domain of the heaving foil

V – 1.2   Structure Domain

The structural analysis numerical domain focuses solely on the internal geometry, eliminating the need to mesh the external domain. Two main geometrical configurations, shown in Figures (8a) and (8b), are tested : the solid model ($S1$) used for rigid analysis, and the hollow model with vertical spars ($S3$) applied for flexible analysis.
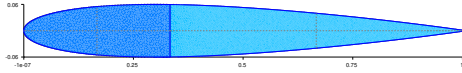
(a) Solid Foil Mesh ($S1$)
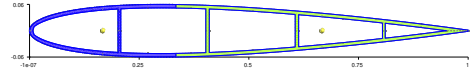
(b) Hollow Spars Foil Mesh ($S3$)
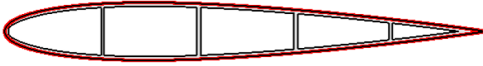
(c)

(d)

FIGURE 8 – (a),(b) Fluid and solid mesh configuration (c) Red nodes indicate the interface between the solid and fluid solvers. (d) The red nodes show the fixation plane at 1/3 of the chord length.

The foil interface surface is shown in Figure (8c), where the integrated forces F_x and F_y are calculated at each time step over a complete heaving cycle and compared to forces from OpenFOAM via the coupled solver in Section (III). For 2D simulations in CalculiX, nodes are confined to the $z = 0$ plane with only x and y translations allowed, and rotations around the z-axis permitted to approximate plane strain condition. A fixation plane at $c/3$ (Figure 8d) constrains node movement and rotation.

V – 2   Kinematics

The wing kinematics are governed by active translation motion applied through the *dynamicMeshDict* in OpenFOAM, using the *solidBodyDisplacementLaplacianSolver*. This solver models the active heaving, with the displacement Laplacian component accurately handling patch displacement as described by $H = h_0 * sin(\omega * t)$ where h_0 and ω are the heaving amplitude (m) and frequency (rad/sec) respectively in the y direction.

V − 3   Material Properties

Material selection is critical for this study. AISI 4000 Series Steel [27] is used for the rigid analysis due to its durability. To investigate flexibility effects, we referenced [1], which found minimal influence from foil thickness but significant impact from material stiffness, particularly with Polyethylene Terephthalate (PET). Thermoplastic Polyurethane (TPU) [28], a flexible material that can be printed in-lab, was also chosen to align with manufacturing constraints. To achieve further flexibility, we selected EL1, a material with a lower Young's modulus. Material properties are listed in Table (4).

Material	Steel	PET	TPU	EL1
Modulus of Elasticity (GPa)	200	5.2	0.026	0.005
Density ($\rho \ kg/m^3$))	7800	2500	1220	1220
Poisson's Ratio (ν)	0.3	0.35	0.35	0.35

TABLE 4 – Material properties for the rigid and flexible materials

V − 4   Propulsion and Energy Harvesting

The thrust output and energy harvesting efficiencies, denoted as η_p and η respectively, for a heaving foil are estimated by averaging the thrust and power coefficients over a complete heaving cycle. These non-dimensional coefficients, represented as $C_{T,\text{mean}}$ and $C_{P,\text{mean}}$, allow for efficiency comparisons. Based on the study by [5], we conclude that :

$$C_{\text{Tmean}} = \frac{1}{T} \int_t^{t+T} C_T(t) \, dt, \quad C_T(t) = \frac{-F_x}{0.5\rho U_0^2} \tag{2}$$

Here, $C_T(t)$ denotes the instantaneous thrust coefficient, calculated as the negative of the drag coefficient. The average power required to drive the airfoil over one flapping cycle is given by :

$$C_{\text{Pmean}} = \frac{1}{T} \int_t^{t+T} C_P(t) \, dt, \quad C_P(t) = -C_L(t)\frac{\dot{y}(t)}{U_0} \tag{3}$$

The vertical displacement and its rate of change are given by :

$$y = h_0 \sin(\omega t), \quad \dot{y}(t) = h_0 \omega \cos(\omega t). \tag{4}$$

The lift coefficient $C_L(t)$ is defined as :

$$C_L(t) = \frac{F_y}{0.5\rho U_0^2} \tag{5}$$

The propulsive efficiency η_p is determined by :

$$\eta_p = \frac{C_{\text{Tmean}}}{C_{\text{Pmean}}}. \tag{6}$$

The efficiency of power extraction, η, is given by :

$$\eta = \frac{P_o}{P_a} = C_{\text{Pmean}}\frac{c}{y_{\text{tot}}}, \tag{7}$$

where $P_a = 0.5\rho U_\infty^3 y_{\text{tot}}$, and y_{tot} is the maximum vertical displacement of the airfoil, typically around $2h_0$.

VI – Results and Discussion

VI – 1   Rigid Heaving Foil

The rigid heaving analysis has two main objectives : (1) to identify operational regimes that optimize performance parameters, thus determining conditions for effective system operation, and (2) to validate FSI solver settings by comparing results with established data from Ashraf et al. [5] and Heathcote and Gursul [19], ensuring the solver's accuracy and reliability for further applications.

The flow parameters are detailed in Table (5), with the primary simulation variables being the non-dimensional displacement amplitude ($h = h_0/c$) and reduced frequency ($k = \omega c/u$). This analysis evaluates the impact of the non-dimensional flapping velocity (kh) on key performance metrics (η and η_p), focusing on time-averaged thrust and power coefficients, propulsive efficiency, and energy harvesting efficiency as functions of kh. Here, kh is varied by adjusting h_0 while keeping $k = 1$. Each simulation generally spans 5 to 20 flapping cycles, with lower amplitudes converging faster. Mean values are derived from the final three cycles, and additional simulations with flexible foils explore flexibility's effects on propulsive and power extraction efficiencies.

Fluid	Value	Solid	Value
Fluid Velocity (u)	0.2007 m/s	Modulus of Elasticity (E)	200 GPa
Fluid Density (ρ_f)	999.1 kg/m^3	Solid Density (ρ_s)	7800 ρ kg/m^3
Characteristic Length (c)	0.1 m	Poisson's Ratio (ν)	0.35
Reynolds number (R_e)	20000		

TABLE 5 – Input Variables and Their Values

In Figure (9), a reasonable agreement is observed between our results, the numerical data from [5], and experimental data from [19]. At very low values of (kh), the thrust generated by the airfoil fails to overcome viscous drag, resulting in a negative propulsive efficiency. As (kh) increases, thrust production surpasses viscous drag, improving propulsive efficiency. However, at higher (kh) values, increased wake formation and trailing edge separation reduce propulsive efficiency.

As shown in Figure (10), increasing the plunge amplitude shifts the time series from periodic to chaotic behavior. Phase plots of C_T and C_L illustrate this transition : for $0.15 < h < 0.5$, aligned plots across cycles indicate periodic force generation. In the range $0.5 \leq h \leq 1$, quasi-periodic behavior emerges with additional frequency content. When $h > 1$, the phase plots lose discernible patterns, signaling chaotic behavior. These observations clarify the amplitude and frequency bounds that support stable heaving responses.
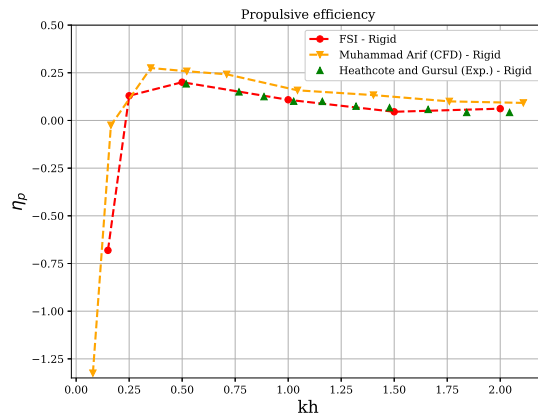

FIGURE 9 – Propulsive efficiency variation with kh. The rigid foil values, evaluated using the overset zone solver, are validated against numerical data from [5] and experimental data from [19].
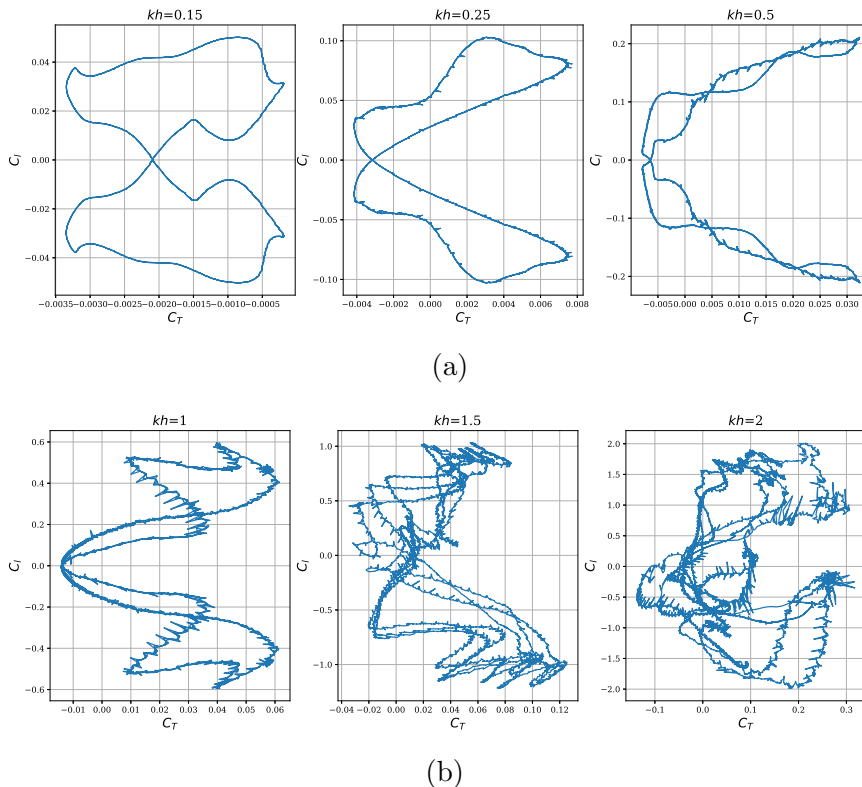
(a)

(b)

FIGURE 10 – Thrust and Power Coefficients History vs. Time with the Variation of kh

VI – 2   Flexible Heaving Foil

We now examine the impact of flexibility on performance by incorporating elasticity through the hollow solid profile, as shown in Figure 8b. Flow conditions remain consistent with those in Table 5, with $Re = 20000$. The heaving kinematics are set at $kh = 1$, where $k = 1$ corresponds to $\omega = 2.007$ rad/s, $T = 3.13$ sec, and $h = 1$ with a maximum amplitude of $h_0 = 0.1$ m. Materials used are specified in Table 4. The previously introduced rigid case is reanalyzed to assess the impact of reduced stiffness on energy harvesting efficiency.

Material	Steel	PET	TPU	EL1
Energy Harvesting Efficiency (η)	0.0992	0.1031	0.1108	0.1218
$\Delta\%\eta$	-	3.93%	11.69 %	22.78 %

TABLE 6 – Energy harvesting efficiency for heaving NACA0012 based on different materials for $kh = 1$ and $R_e = 20000$ using S_3 model

As illustrated in Figure (11a), during the initial phase of the flapping cycle ($t/T = 0 - 0.2$), the power coefficient (C_P) for the two most rigid cases (Steel and PET) are almost identical. In contrast, TPU and $EL1$ exhibit noticeable differences, with EL1 displaying a larger area under the curve, indicating a higher C_P. At the midpoint of the cycle ($t/T = 0.5$), PET outperforms Steel in C_P, demonstrating where flexibility enhances power output. A similar trend appears with the more flexible materials, where C_P increases from TPU to $EL1$, reflecting enhanced power extraction with increased flexibility.

The translation motion amplitude versus time plot is shown in Figure (11b), where the start of the heaving cycle at $t/T = 0$ aligns with the end of the previous cycle at $t/T = 1$.
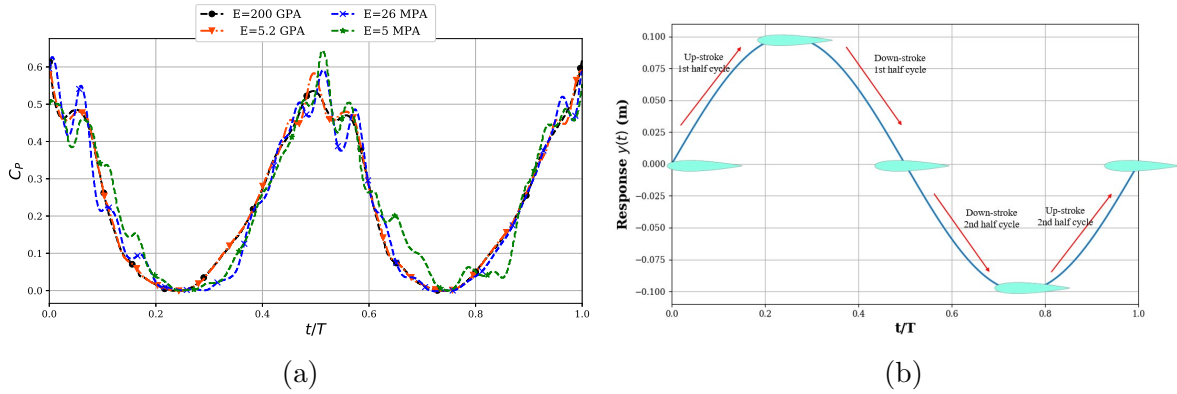
FIGURE 11 – (a) The effect of flexibility on the power coefficient for $kh = 1$ and $R_e = 20000$ using S_3 model. (b) Translation amplitude Vs t/T for $kh = 1$

Each cycle includes two up-strokes ($t/T = 0 - 0.25$ and $t/T = 0.75 - 1$) and two down-strokes ($t/T = 0.25 - 0.5$ and $t/T = 0.5 - 0.75$). The evolution of the LEV and TEV over a complete heaving cycle is depicted in Figure (12). At $t/T = 0$, a new LEV forms while a previously shed LEV remains near the lower foil surface, approximately a quarter chord length downstream. During the upstroke at $t/T = 1/4$, the LEV detaches, convects along the foil, and sheds into the wake, leaving a trailing-edge shear layer by $t/T = 1/2$. This behavior aligns with [26], [37], and [24], indicating that flapping wings sustain LEVs due to pressure gradients and non-inertial forces during down-strokes, creating a low-pressure zone that enhances lift. To illustrate the impact of foil flexibility on power harvesting, we analyze Z-vorticity for foils with $E = 5$ MPa and $E = 5.2$ GPa in Figure (13). From $t/T = 0.375$ to $t/T = 0.75$, during the down-stroke, the LEV on the ($EL1$) foil sheds earlier than on the (PET) foil , stretching faster toward the TE. This generates a stronger adverse pressure gradient on the upper surface, leading to a larger suction zone, which enhances lift and power extraction.

The vertical displacements at the leading edge (y_{LE}) and trailing edge (y_{TE}) of the foils over a heaving cycle are shown in Figure(14), along with the Fast Fourier Transform (FFT) of the response to evaluate deformation frequency. Under pressure forces from heaving in water, the $EL1$ foil shows notable bending, with LE peaks of $y_{LE} = 5.14$ mm between $t/T = 0.4 - 0.6$ and TE peaks of $y_{TE} = 3.4$ mm between $t/T = 0.4 - 0.7$. The TPU foil reaches maximum deflections at the cycle midpoint, with $y_{LE} = 1$ mm and $y_{TE} = 0.54$ mm. The PET foil, being stiffer, experiences minimal deformation, peaking at $y_{LE} = 0.004$ mm and $y_{TE} = 0.002$ mm, also at the cycle midpoint. FFT analysis reveals the dominant deformation frequency at $f_d = 0.319$ Hz for all materials, aligning with the flapping motion frequency $\omega = 2.007$ rad/s ($T = 3.13$ s). This consistency implies that foil deformations are primarily driven by the flapping frequency, with no additional higher-frequency oscillations significantly impacting the response.To enable realistic water tunnel testing, a modified solid design (S_4) was developed, as S_3 was challenging to handle. Design S_4 includes a circular section within the foil, providing housing for a supporting rod that transmits motion while reinforcing the structure. The rod's center is located at $x/c = 1/3$, aligning with the fixation point. A TPU prototype of the S_4 foil, produced by our manufacturing team, is shown in Figure(15a). The η of the S_4 foil with TPU was compared to the S_3 foil under identical conditions ($Re = 20000$, $kh = 1$, $k = 1$, $\omega = 2.007$ rad/s). Results show S_4 achieved $\eta = 0.1152$, representing a 16.13% improvement over the rigid case and surpassing the S_3 foil, which achieved an 11.69% increase.
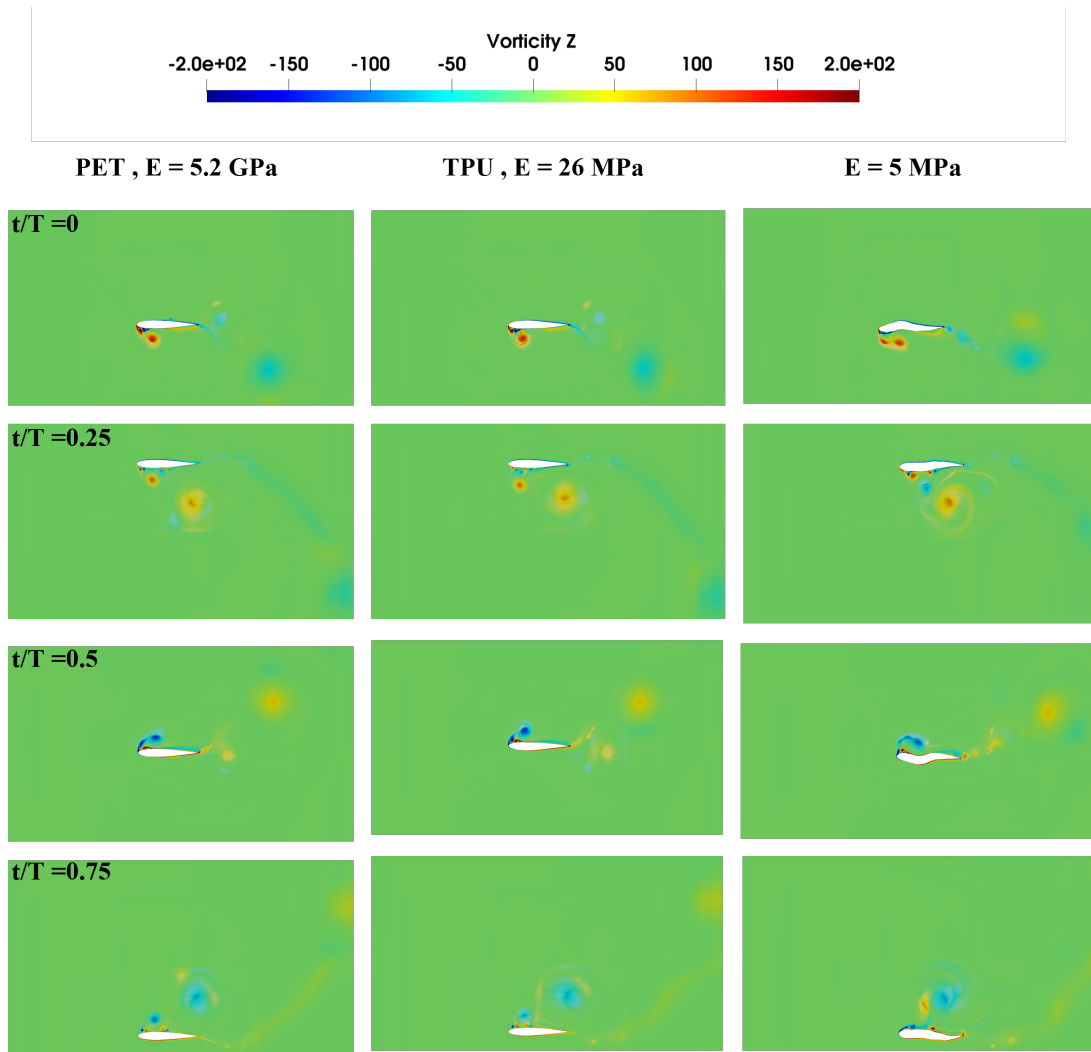
13

FIGURE 12 – Z-Vorticity contours vs T/t for various material at $kh = 1$ and $R_e = 20000$

(a) *Steel*, $t/T = 0.375$ (b) $t/T = 0.5$ (c) $t/T = 0.625$ (d) $t/T = 0.75$

(e) *EL1*, $t/T = 0.375$ (f) $t/T = 0.5$ (g) $t/T = 0.625$ (h) $t/T = 0.75$
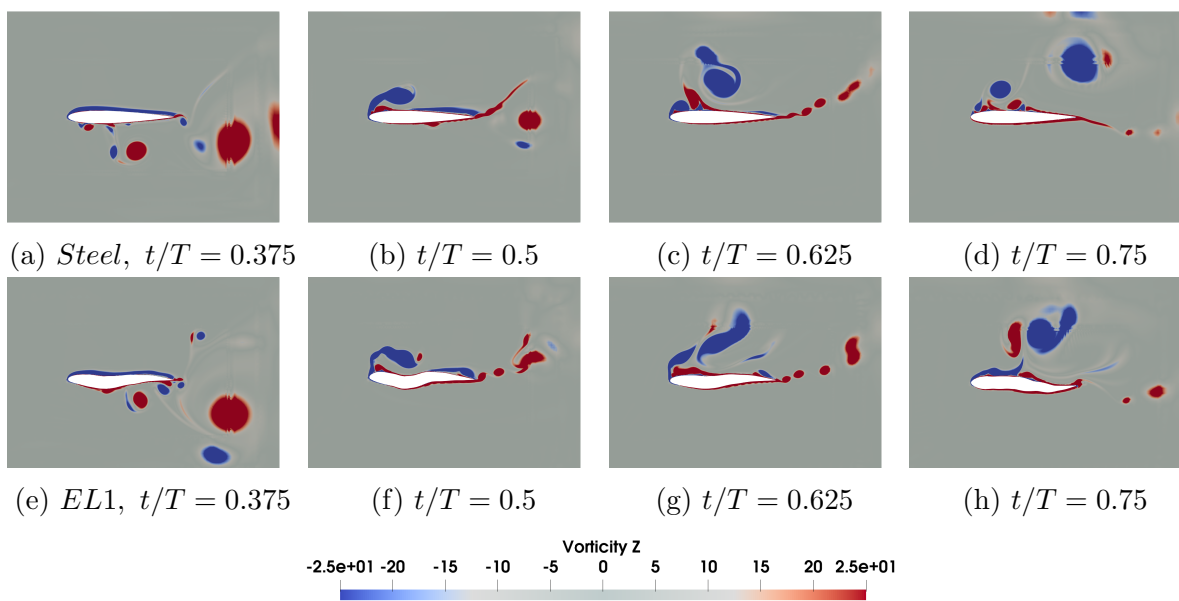
FIGURE 13 – Z-Vorticity contours for case of *Steel* and *EL1* at the down-stroke phase
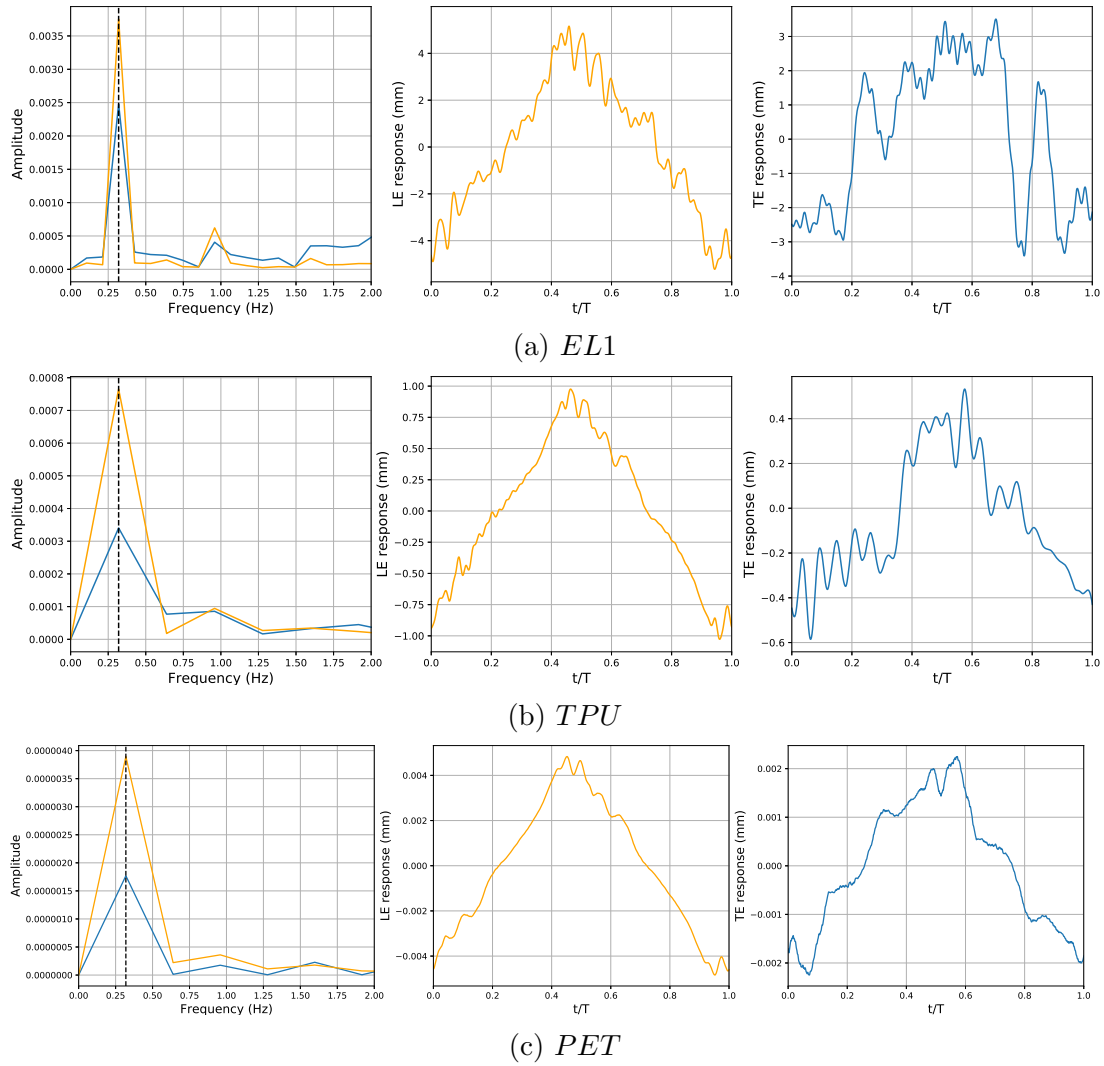
FIGURE 14 – Fast fourier transform and magnitude of the leading edge and trailing edge deformation over a complete heaving cycle for various materials
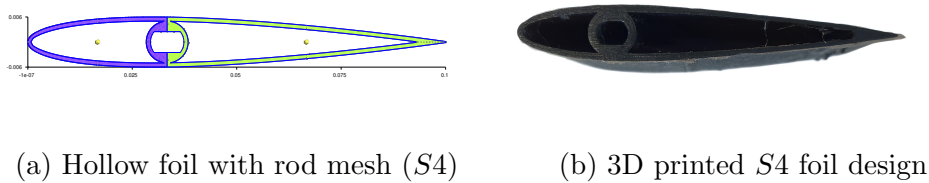

(a) Hollow foil with rod mesh ($S4$)   (b) 3D printed $S4$ foil design

FIGURE 15 – S3 and S4 Solid mesh configuration

VII – Conclusions and Perspectives

In this study, we developed a coupled fluid-structure interaction (FSI) solver that integrates our previously developed overset zone solver with the solid solver CalculiX, facilitated through the preCICE coupling library. The overset zone technique was employed to handle the complex fluid flow and mesh motion and deformation, while CalculiX was utilized for structural analysis. This framework was validated by solving benchmark pro-

blem and verified with published literature, which confirmed the solver's reliability for both rigid and flexible body simulations.

The solver was applied to analyze propulsion generation and energy harvesting in heaving foils. Initially, we investigated the behavior of rigid foils, showing good agreement with existing data and highlighting the impact of increasing flapping amplitude on transitioning from periodic to chaotic behavior. Allowing us to have a clear indication on the upper and lower limit of our working regime concerning the heaving amplitudes and frequencies. Subsequently, flexible foils with varying stiffness were analyzed. The results demonstrated that increasing material flexibility significantly enhances energy harvesting efficiency. It was observed that, during the heaving cycle, the more flexible foils exhibited greater deformation at both the leading and trailing edges, particularly during the critical phases of the cycle. The most flexible foil showed earlier and stronger vortex shedding, which resulted in an increased adverse pressure gradient and enhanced lift. The vertical displacement of the flexible foil was substantially higher than that of the more rigid foils, leading to an overall increase in the energy extracted from the flow. FFT analysis confirmed that the deformations in all tested foils were primarily driven by the fundamental flapping frequency, with no evidence of higher frequency oscillations influencing the response. This highlights the role of flexibility in promoting a more efficient energy harvesting process by strengthen the interaction between the fluid and the foil.

One of the key developments was the design of the S_4 foil, which incorporates a practical housing for experimental setups. This design achieved better energy harvesting performance than the earlier S_3 model, providing promising insights for future experimental validations.

Looking forward, we aim to test the existed foil experimentally in water tunnel facilities to further validate the simulation results. Moreover, future work will focus on exploring new foil designs to optimize energy harvesting efficiency. Additionally, we plan to implement a passive motion solver based on the 6-degree-of-freedom (6DOF) solver in OpenFOAM, incorporating spring stiffness and damping coefficients, with the goal of developing a fully passive system. This progression will allow for the design of an efficient and optimized hydro-elastic energy harvester.

Références

[1] Effect of flexural stiffness on the aerodynamic forces of flapping mavs, 2010.

[2] Numerical benchmarking of fluid-structure interaction between an elastic object and laminar incompressible flow. 2018.

[3] Configuration acceleration — precice documentation, 2024.

[4] K. Ahmed, A. A. Hamada, L. Chatellier, and M. Furth. A modified overset method in openfoam for simultaneous motion and deformation : A case study of a flexible flapping foil. *OpenFOAM® Journal*, 4 :41–61, Apr. 2024.

[5] M. A. Ashraf. *Numerical simulation of the flow over flapping airfoils in propulsion and power extraction regimes*. PhD thesis, UNSW Sydney, 2010.

[6] E. Atta. Component-adaptive grid interfacing. In *19th Aerospace Sciences Meeting*, page 382, 1981.

[7] T. J. Baker. Mesh generation : Art or science ? *Progress in Aerospace Sciences*, 41(1) :29–63, 2005.

[8] J. Benek, P. Buning, and J. Steger. A 3-d chimera grid embedding technique. In *7th Computational Physics Conference*, page 1523, 1985.

[9] J. Benek, T. Donegan, and N. Suhs. Extended chimera grid embedding scheme with application to viscous flows. In *8th Computational Fluid Dynamics Conference*, page 1126, 1987.

[10] J. Benek, J. Steger, and F. C. Dougherty. A flexible grid embedding technique with application to the euler equations. In *6th computational fluid dynamics conference Danvers*, page 1944, 1983.

[11] G. Chourdakis. A general openfoam adapter for the coupling library precice. Master's thesis, Technical University of Munich, 2017.

[12] W. Dynamics. Moving bodies and dynamic meshes in openfoam. https ://www.wolfdynamics.com/training/movingbodies/OF2021, 2021.

[13] J. Falnes. A review of wave-energy extraction. *Marine structures*, 20(4) :185–201, 2007.

[14] E. Farrell Helbling and R. J. Wood. A Review of Propulsion, Power, and Control Architectures for Insect-Scale Flapping-Wing Vehicles. *Applied Mechanics Reviews*, 70(1), Jan. 2018.

[15] A. A. Hamada and M. Fürth. Ground effect on current energy harvesting from a freely-oscillating circular cylinder at low reynolds number. In *International Conference on Offshore Mechanics and Arctic Engineering*, volume 85192, page V009T09A003. American Society of Mechanical Engineers, 2021.

[16] A. A. Hamada and M. Fürth. Numerical investigation of the energy harvesting capabilities of naca series flapping foil turbines in swing-arm mode. *SSRN Electron. J.*, 2022.

[17] K. Hargroves and M. H. Smith. Innovation inspired by nature biomimicry. *Ecos*, (129) :27–30, 2006.

[18] S. Heathcote and I. Gursul. Flexible flapping airfoil propulsion at low reynolds numbers. *AIAA journal*, 45(5) :1066–1079, 2007.

[19] S. Heathcote and I. Gursul. Flexible flapping airfoil propulsion at low reynolds numbers. *AIAA Journal*, 2007.

[20] C. W. Hirt, A. A. Amsden, and J. Cook. An arbitrary lagrangian-eulerian computing method for all flow speeds. *Journal of computational physics*, 14(3) :227–253, 1974.

[21] W. Ibrahim, M. Mohamed, R. Ismail, P. Leung, W. Xing, and A. Shah. Hydrokinetic energy harnessing technologies : A review. *Energy Reports*, 7, 2021.

[22] T. Jardin, A. Farcy, and L. David. Three-dimensional effects in hovering flapping flight. *Journal of fluid mechanics*, 702 :102–125, 2012.

[23] H. Jasak and Ž. Tuković. Dynamic mesh handling in openfoam applied to fluid-structure interaction simulations. In *Proceedings of the V European Conference on Computational Fluid Dynamics ECCOMAS CFD 2010*, 2010.

[24] T. Kinsey and G. Dumas. Parametric study of an oscillating airfoil in a power-extraction regime. *AIAA journal*, 46(6) :1318–1330, 2008.

[25] P. Laws, J. S. Saini, and A. Kumar. A study on openfoam's overset mesh support using flow past naca 0018 airfoil. preprint on webpage at https ://www.preprints.org/manuscript/201907.0217/download/final$_f ile$, 2019.

[26] W. Liu, Q. Xiao, and F. Cheng. A bio-inspired study on tidal energy extraction with flexible flapping wings. *Bioinspiration & biomimetics*, 8(3) :036011, 2013.

[27] MatWeb. Aisi 4000 series steel, 2024. Material Data Sheet.

[28] MatWeb. Material data sheet for thermoplastic polyurethane, 2024.

[29] K. Patel, K. Supradeepan, and P. Gurugubelli. A numerical study on the flapping dynamics of a heaving flexible foil in a uniform flow. In *Theoretical, Computational, and Experimental Solutions to Thermo-Fluid Systems : Select Proceedings of ICITFES 2020*, pages 149–158. Springer, 2021.

[30] D. Risseeuw. Fluid structure interaction modelling of flapping wings : Development and validation of a general open-source fluid structure interaction method with analysis of flexible flapping wing aerodynamics. 2019.

[31] J. Rose, S. G. Natarajan, and V. Gopinathan. Biomimetic flow control techniques for aerospace applications : a comprehensive review. *Reviews in Environmental Science and Bio/Technology*, 20(3) :645–677, 2021.

[32] SimFlow. Over pimple and dymfoam, 2024. Accessed : 2024-08-28.

[33] P. Tisovska. Description of the overset mesh approach in esi version of openfoam. *Proceedings of the CFD with OpenSource Software*, 2019.

[34] S. Turek and J. Hron. *Proposal for numerical benchmarking of fluid-structure interaction between an elastic object and laminar incompressible flow*. Springer, 2006.

[35] S. Turek and J. Hron. Proposal for Numerical Benchmarking of Fluid-Structure Interaction between an Elastic Object and Laminar Incompressible Flow. In *Fluid-Structure Interaction*, Lecture Notes in Computational Science and Engineering, Berlin, Heidelberg, 2006. Springer.

[36] B. Uekermann, H.-J. Bungartz, L. C. Yau, G. Chourdakis, and A. Rusch. Official precice adapters for standard open-source solvers. In *Proceedings of the 7th GACM colloquium on computational mechanics for young scientists from academia*, 2017.

[37] Q. Xiao, W. Liao, S. Yang, and Y. Peng. How motion trajectory affects energy extraction performance of a biomimic energy generator with an oscillating foil ? *Renewable energy*, 37(1) :61–75, 2012.

[38] F. Xie, Q. Zuo, Q. Chen, H. Fang, K. He, R. Du, Y. Zhong, and Z. Li. Designs of the biomimetic robotic fishes performing body and/or caudal fin (bcf) swimming locomotion : a review. *Journal of Intelligent & Robotic Systems*, 102(1) :1–19, 2021.